3.1
NMR Spectroscopy in Electrochemistry

YuYe Tong
Georgetown University, Washington, Washington DC

Eric Oldfield and Andrzej Wieckowski
University of Illinois at Urbana-Champaign, Urbana, Illinois

3.1.1
Introduction

The fundamental physical origins of the different chemical reactivities of catalytic or functional metal surfaces – be they used as heterogeneous catalysts, electrocatalysts, substrates for materials engineering, or simply as templates for corrosion studies – are electronic [1]. Most surface processes can be considered to involve the optimization of the electronic interaction energy of the system through suitable geometric rearrangements. These surfaces processes necessarily involve the activation of one or more chemical ingredients together with the concomitant excitation of the many-electron metal surface. They are, therefore, in general rather complex processes.

In the gas (dry) phase, ultrahigh vacuum (UHV)-based surface science characterization techniques have been developed for many years for scrutinizing complex surface processes [2]. Unfortunately, few of these techniques are readily applicable to investigating problems at the electrochemical interface, because of the ubiquitous presence of the condensed-phase electrolyte. In electrocatalysis/fuel cell applications, for instance, specific chemical and physical properties of the electrode become of paramount importance in terms of understanding the fundamental aspects of such interfacial electrochemical phenomena [3]. It is in this field of interfacial electrochemistry that the newly developed electrochemical nuclear magnetic resonance (EC-NMR) spectroscopy technique [4] is mainly applicable. This development is now beginning to bring results that illuminate both electronic and dynamic aspects of processes in real-world catalytic systems [4–10].

Technically, however, NMR probably possesses the lowest mass-detection sensitivity of any spectroscopic technique [11] and is still quite a challenging prospect. To appreciate the difficulties, note that a typical high-field NMR instrument needs $\sim 10^{18}-10^{19}$ NMR-active atoms, for example ^{13}C spins, to make a signal detectable within a reasonable time period. However, 1 cm^2 of a single-crystal metal surface contains only about 10^{15} atoms. Therefore, at least 1 m^2 surface area of NMR-active

atoms is needed to meet the sensitivity requirement, which is the primary reason that most surface NMR investigations reported so far have used high-surface-area materials. Nevertheless, there are several advantages to using NMR to investigate (electrochemical) surface processes. For example, NMR is extremely sensitive to local static (geometric), electronic, and dynamic structure [12]. Also, NMR can characterize samples in most types of catalysts – metal powders, oxide-supported metal catalysts, carbon-supported catalysts, and both metal and adsorbate structures can be probed. In addition, it is a nondestructive technique and can be applied under technically demanding environmental conditions close to real-world operating conditions. For example, it is possible to investigate graphite-supported metal catalysts in an electrochemical environment under potential control. Given adequate mass sensitivity then, NMR has a unique ability to provide a wealth of electronic and structural information on the atomic level, and in addition permits one to access motional information on adsorbates over a time-span unattainable by any other spectroscopic technique. As such, NMR of oxide-supported metal catalysts has therefore played an important historical role in the development of many fundamental aspects of gas-phase heterogeneous catalysis at transition metal surfaces [13–16], and the techniques developed, primarily by Slichter and coworkers [17], can be readily adapted to electrochemical systems.

EC-NMR was pioneered by Wieckowski's group [18] at the University of Illinois at the beginning of 1990s and, as noted above, has its roots in metal NMR of oxide-supported metal catalysts. However, interfacing solid-state NMR with interfacial electrochemistry is somewhat more challenging than the more standard "gas-phase" techniques because of the basic incompatibility between NMR detection and the conducting requirements for proper electrode function. That is, the presence of conducting material in the NMR-detection coil greatly degrades the so-called quality factor of the NMR probe, which substantially decreases sensitivity. Nevertheless, the potential advantages of interfacing in situ solid-state NMR with electrochemistry for investigating the electrochemical interface are many. For example: NMR gives a direct probe of the Fermi level local densities of states – for both adsorbate and substrate; structure and bonding in an electrochemical environment can be investigated using a variety of NMR interactions; surface dynamics can be readily probed; and, of course, the effects of potential control can be investigated in working electrochemical systems – even where the adsorbates (such at CN on Pt) would not be accessible in conventional "gas-phase" or dry systems. Furthermore, by using high magnetic fields and high-surface-area electrode materials, the current state-of-the-art signal-detection sensitivity is in fact quite reasonable, and permits the routine acquisition of NMR spectra of surface species. As an example, we show in Fig. 1 ^{13}C NMR spectra of ^{13}CO chemisorbed onto a 10-nm Pt sample having a CO coverage of about 0.8, recorded at room temperature and in, respectively, Fig. 1(a), 14.1 and Fig. 1(b), 8.5 T magnetic fields. The numbers of scans were 1600 and 2000, and the signal-to-noise (S/N) ratios (after using a 1-kHz line broadening) were 50 and 10, respectively, showing a significant S/N enhancement in the higher magnetic field. Sensitivity is also greatly enhanced at lower temperatures at which ^{13}C NMR spectra can now be recorded in as little as 10 min.

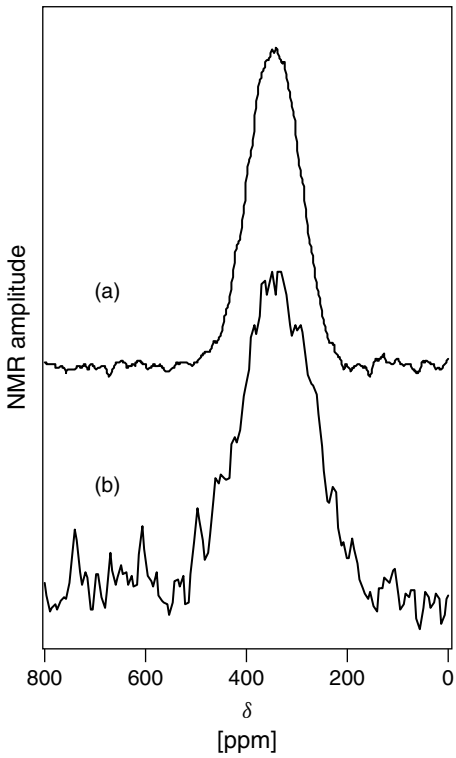

Fig. 1 ^{13}C NMR spectra of CO adsorbed on a 10-nm Pt electrocatalyst, recorded at room temperature and at (a) 14.1 T with 1600 scans and (b) 8.5 T with 2000 scans. The S/N ratios are ca. 50 and 10, respectively.

3.1.2 Principles of Solid-state Surface EC-NMR Spectroscopy

3.1.2.1 Metal NMR Basics

In electrochemistry, electrodes are indispensable parts of an electrical circuit, so the EC-NMR of electrode surfaces in general has to deal with metallic systems. In NMR, in general, a specific resonance position (a frequency shift) with respect to a well-defined reference corresponds to a specific chemical environment (a structure) [12]. This shift is the chemical shift (δ_{CS}) in a molecule or the Knight shift (K) [19] in a metal, and can be considered a fingerprint of the corresponding site or structure [20]. While the familiar chemical or orbital shift is ubiquitous, arising from the shielding of the external magnetic field at the nucleus by the otherwise quenched orbital angular momentum of the surrounding electrons, the Knight shift is metal-specific, being produced by nonzero magnetic interactions between nuclear and electronic spins since only electron spins at the Fermi energy can be polarized and thus create a nonzero spin density in an external magnetic field (the so-called Pauli paramagnetism). In addition, the Korringa relationship [21] (vide infra), which governs the nuclear spin–lattice relaxation in metals, is also metal-specific. Together, the Knight shift and the Korringa relation represent the two primary NMR probes of electronic structure in metals, and of surface molecular bonding in general.

Theoretically, the Hamiltonian of the nuclear–electron hyperfine interaction can be written for a nuclear spin $I = 1/2$ as

$$H = \gamma_n \hbar I \mu_B \left\{ \frac{8\pi}{3} S(r)\delta(r) - \left[\frac{S}{r^3} - \frac{3r(Sr)}{r^5} \right] - \frac{\ell}{r^3} \right\} \quad (1)$$

where μ_B is the Bohr magneton and γ_n is the nuclear gyromagnetic ratio. I, S, and l are the nuclear spin, electron spin, and electron orbital moments, respectively. The symbol r is the radius vector of an electron with respect to the nucleus at the origin. The first term in the brace in Eq. (1) is the Fermi contact term, the second (square bracket) is the dipole term, and the third (l/r^3) is due to the orbital movement of electrons. In a diamagnetic molecule,

since all electron spins are paired up, the expectation values of the first and second terms become zero, leaving only the third term, which produces the usual so-called chemical or orbital shift, δ_{CS}. In the case of a metal, the total line shift is the *sum* of the first term (K) and the third term (δ_{CS}) in Eq. (1). In many cases, K, which arises from the hyperfine interaction of the observed nucleus with electron spins, dominates the purely chemical shift term, δ_{CS}. The dipolar term normally contributes to relaxation, but not to the shift, since the trace of the operator is zero.

The Korringa relationship [21] indicates that $1/T_1 \propto T$, where T_1 is the spin–lattice relaxation time and T is the absolute temperature of the sample. This unique temperature dependence of $1/T_1$ is the NMR fingerprint of a metallic state. It results from the fact that only conduction electrons around the Fermi level can satisfy energy conservation for the electron-nuclear spin "flip-flop" relaxation process, and the fraction of these electrons is proportional to $k_B T$. When all relaxation mechanisms other than the first term in Eq. (1) can be neglected, and there are only s-like electrons at the Fermi level (such as in the alkali metals), the Korringa relationship takes its simplest form:

$$K^2 T_1 T = \left(\frac{\gamma_e}{\gamma_n}\right)^2 \left(\frac{h}{4\pi k_B}\right) = S \qquad (2)$$

Here, γ_e and γ_n are the electronic and nuclear gyromagnetic ratios, respectively, and k_B is the Boltzmann constant. The Knight shift, K, also has a simple relationship with the electronic density of states at the Fermi level through the Pauli susceptibility, χ_{Pauli}:

$$K = \chi_{Pauli} \frac{H_{hf}}{\mu_B} = \mu_B H_{hf} D(E_F) \qquad (3)$$

where H_{hf} is the hyperfine field produced by an electron at the site of the nucleus, and $D(E_F)$ is the (local) density of states at the Fermi level. Despite their simplicity, Eqs. (2 and 3) already give the simple physical picture that the NMR of metallic species can measure, in principle, $D(E_F)$. For systems having more than one band, which cuts the Fermi level, the deduction of multiple $D(E_f)$s becomes more involved, though the principles are the same. More specifically, for ^{195}Pt [22] or chemisorbed ^{13}CO [10], one can express the two primary metal NMR observables, the Knight shift K and the Korringa constant $S(T_1T)^{-1}$, in terms of $D(E_F)$s. This is the so-called two-band model, the bands corresponding to metal s and d bands or to ligand (^{13}CO) 5σ and $2\pi^*$ bands. By experimentally measuring K and $S(T_1T)^{-1}$ (for the metal or ligand) and by solving two equations for two unknowns, s (5σ)- and d ($2\pi^*$)-$D(E_F)$ can be deduced. For more details, the reader is referred to Refs. [10, 20, 22].

It is important to note that many metallic properties, such as the Knight shift and the Korringa relationship, are determined by the finite and quasi-continuous nature of the Fermi level local density of states (E_F-LDOS). In the approximation most familiar to chemists, what this means is that the highest occupied molecular orbital–lowest unoccupied molecular orbital (HOMO–LUMO) gap in metals is much smaller than the thermal energy $k_B T$, and the value of the E_F-LDOS reflects the frontier orbital contributions in a metallic system [23]. The E_F-LDOS also represents a crucial metal surface attribute that can serve as an important conceptual bridge between the delocalized band structure (physics) picture and the localized chemical bonding (chemical) picture of metal–adsorbate interactions.

In addition to the determination of the chemical and/or Knight shift and the spin–lattice relaxation time in the laboratory frame (T_1), there is another important NMR observable – the spin–spin relaxation time (T_2). While the chemical and/or Knight shift contains essentially static structural information, the temperature and/or magnetic field dependence of the relaxation times, both T_1 and T_2, are related to the dynamics of the observed nucleus. T_1 measures the rate at which the spin system returns to thermal equilibrium with its environment (the lattice) after a perturbation, while T_2 measures the rate of achieving a common spin temperature within the spin system. Both T_1 and T_2 provide exceptionally important information on motions, and can cover the timescale from $\sim 10^{-9}$ to 10^2 s. Moreover, the temperature dependence of these motions provides important thermodynamic information in the form of activation energies for ligand motion on the catalyst surface.

3.1.2.2 EC-NMR Instrumentation

Two types of EC-NMR experiments have been carried out: electrode potential–dependent studies of an adsorbate (^{13}CO, ^{13}CN) at room temperature [6, 8, 24], and temperature-dependent studies of an adsorbate [5, 10] and of platinum electrocatalysts [7, 25], down 10 K. For all of the EC-NMR measurements, the electrode materials, either polycrystalline platinum black or carbon-supported commercial fuel cell grade platinum electrodes, were immersed in a supporting electrolyte, typically 0.5 M H_2SO_4. For temperature-dependence studies, EC-NMR samples are prepared in a conventional three-electrode flow cell with oxygen-free N_2 or Ar as a protecting gas, then together with supporting electrolyte and under the protection of oxygen-free N_2 or Ar, are transferred into a precleaned glass ampoule and flame-sealed. The potential drift of a sample in a conventional three-electrode cell, in an oxygen-free environment, is only a few millivolts over 12 h. The same observation holds after transferring the electrode material from the NMR ampoule back into the cell. These observations suggest that the surface potential does not change significantly once a sample is sealed (and does not change at all when the sample is frozen).

For room temperature electrode potential–dependence studies, we have incorporated an electrochemical cell inside the NMR probe [6]. This permits running NMR measurements while an (variable) external electrode potential is applied. Figure 2 shows a picture of a real EC-NMR probe as well as a schematic diagram of the setup. The working electrode material was loosely packed in the cell that was placed inside an NMR coil and electrical connection to an external circuit (potentiostat) made by inserting a Pt wire into the sample. (A very similar setup has also been developed by the Lausanne group [8, 24].) Our cell design permits both electrochemical sample preparation and characterization (voltammetry) and NMR data acquisition under active potential control, avoiding sample transfer from the preparative electrochemical cell. A very important technical issue here is that while the potentiostat is on, there is considerable "noise" injected into the NMR probe, since the potentiostat leads act as excellent "antennas" right inside the NMR coil! This noise has to be removed by using extensive electronic filtering of the electrochemical leads entering the probe, in order to eliminate extensive radio frequency (rf) pickup. The low-pass filter circuit elements $L_{\text{counter}}C_{\text{counter}}$, $L_{\text{ref.}}C_{\text{ref.}}$, and $L_{\text{wk.}}C_{\text{wk.}}$

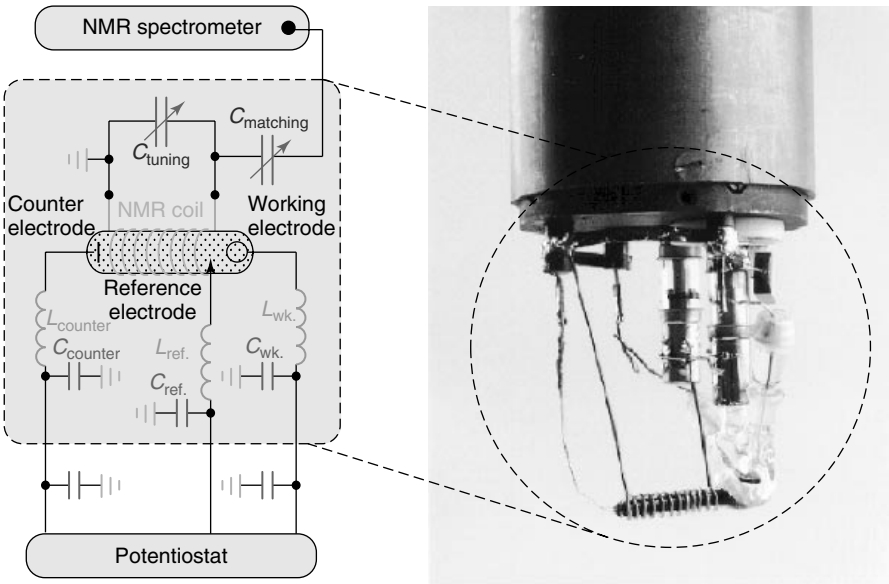

Fig. 2 Schematic diagram (left) and picture (right) of an EC-NMR probe and its circuitry, showing the interface between NMR and electrochemistry.

in Fig. 2 were designed for this purpose, plus they serve a second purpose of acting as a high impedance to the rf pulses from the NMR spectrometer. These are typically ~1 kW and may be incompatible with long potentiostat life.

Figure 3 shows another type of setup for an EC-NMR cell, developed by the Berkeley group to investigate ^{13}CO adsorption from the gas phase onto a carbon-supported platinum electrocatalyst [26, 27]. In this system, a platinum electrocatalyst was pressed into a graphitized carbon cloth that was then cut into pieces and stacked into a cylindrical form that fits snugly into the cell's compartment. In order to reduce degradation in the quality factor of the NMR coil due to the presence of bulk electronic or ionic conductivity, the electrode layers were also alternately sandwiched with nonconductive fiberglass cloth. All the electrode layers were individually stitched with gold wire and were then connected to each other and to the external potentiostat. Cyclic voltammograms of high quality are obtained by both types of EC-NMR cell.

3.1.3 Applications of Solid-state Surface EC-NMR Spectroscopy

3.1.3.1 ^{195}Pt NMR of Carbon-supported Electrocatalysts and a Potential-scan-generated Sintering Effect

At the beginning of the 1980s, Slichter and coworkers discovered several unique features of the ^{195}Pt NMR of oxide-supported small platinum particles [28]. They found that the overall ^{195}Pt NMR lineshape was extremely broad, extending downfield some 4 kG from the position of bulk platinum (1.138 G kHz^{-1}), and contained a feature on the low-field side (1.089 G kHz^{-1}), which arose from the oxidized Pt surface atoms. Later on, van

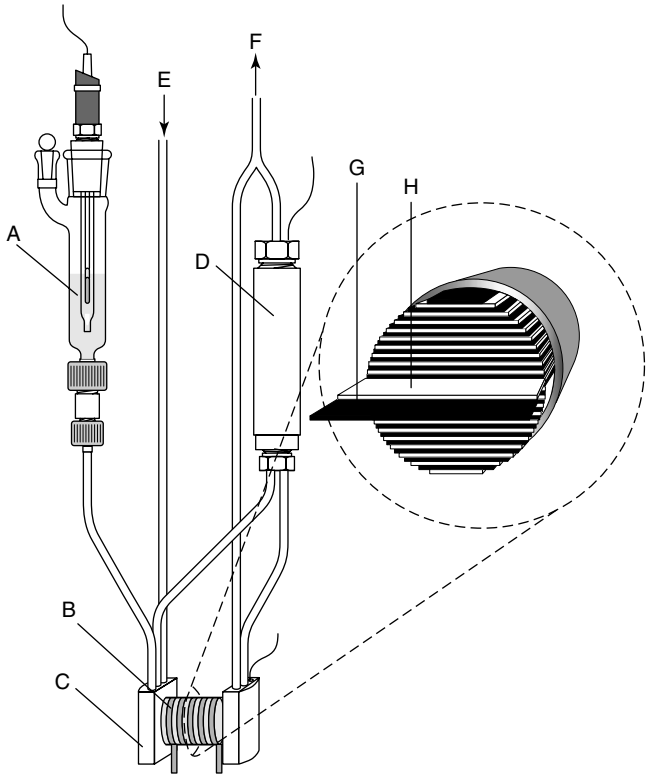

Fig. 3 Schematic representation of the EC-NMR probe cell developed by the Berkeley group [27]: (A) reference electrode compartment; (B) NMR coil; (C) working electrode compartment; (D) counterelectrode compartment; (E) electrolyte inlet; (F) electrolyte outlet; (G) carbon-supported Pt electrocatalysts; and (H) fiberglass separator. (Reproduced with permission from Ref. [27], Copyright by © 2001 Electrochemical Society.)

der Klink and coworkers confirmed these observations, finding that the signal from clean-surface Pt atoms was centered at 1.100 G kHz^{-1} [29], a position clearly very different to the 1.138 G kHz^{-1} bulk position (the frequency difference is magnetic field dependent and is about 2.5 MHz in a field of 8.5 T). Ab initio theoretical calculations on a five-layer Pt (001) cluster [40] then demonstrated that the surface shift must be due to a gradual drop in the d-like Fermi level LDOS on moving from the inside of the particle to the surface. It is this distinguishable surface signal that makes ^{195}Pt NMR unique in investigating the surface physics and chemistry of nanoscale platinum particles.

We have observed that carbon-supported nanoscale platinum electrodes retain quite closely the ^{195}Pt NMR spectral characteristics of isolated small platinum particles supported on oxides [4, 7, 25, 30], with the clean-surface platinum atoms also resonating at 1.100 G kHz^{-1} with respect to the value for bulk atoms, 1.138 G kHz^{-1}. We show in Fig. 4(a–c), ^{195}Pt NMR spectra

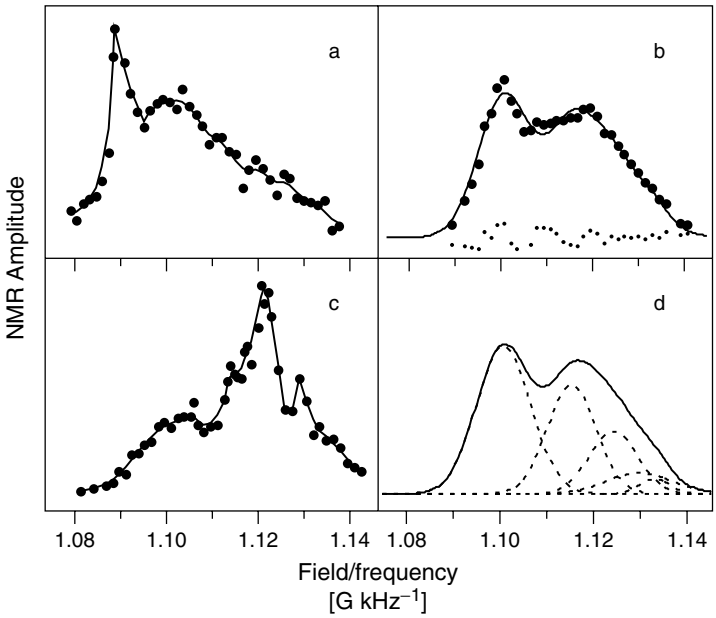

Fig. 4 Typical point-by-point ^{195}Pt NMR spectra showing electrochemical cleaning, sintering by potential cycling, and a layer-model analysis of the 2.5-nm sample: (a) as-received catalyst; (b) electrochemically cleaned in 0.5 M H_2SO_4 by holding electrode potential at 0.45 V versus reversible hydrogen electrode (RHE); (c) cleaned by extensive potential cycling; and (d) layer-model deconvolution of spectrum (b). The solid line in (b) is the result of the simulation.

of a 2.5 nm carbon-supported commercial Pt electrocatalyst after different surface treatments. Figure 4(a) shows the spectrum of an as-received sample, while Fig. 4(b) shows a sample that has been electrochemically cleaned by holding the electrode potential within the electrochemical double-layer region with no potential cycling until the reduction current could no longer be measured. Figure 4(c) shows the spectrum obtained after extensive potential cycling (which is still widely used to clean electrode surfaces), and in which there are clearly discernable spectral differences, as discussed below.

In order to further analyze these results, we use a layer-model [31] (vide infra) deconvolution of the lineshape, and results for the clean-surface spectrum (Fig. 4b) are shown in Fig. 4(d). The NMR layer model assumes that the nanoscale platinum particles can be represented by ideal cubo-octahedral particles built up layer-by-layer from a central atom, that NMR signals from atoms within a given layer can be approximated by a Gaussian, and that the average Knight shift of the nth layer, K_n, which is the center of the corresponding Gaussian, "heals" back exponentially towards the bulk platinum position when moving inwards. That is,

$$K_n = K_\infty + (K_0 - K_\infty)\exp\left(\frac{-n}{m}\right) \quad (4)$$

where n is the layer number, counting inwards from the surface layer (where

$n = 0$), m is the characteristic number (of layers) defining the "healing length" for the Knight shift, and K_0 and K_∞ (= 3.34%) are the Knight shifts of the surface layer and the bulk, respectively. The relative contribution of each Gaussian is dictated by the fraction of the atoms within the corresponding layer, which can be determined from the size distribution of the sample. The healing length, defined as m times the distance between two consecutive layers (0.229 nm for Pt), is 0.46 nm (≅2 Pt layers) from the deconvolution shown in Fig. 4(d). In addition, the shape of a ^{195}Pt NMR spectrum conveys information on the size of the electrocatalyst. That is, the stronger is the surface peak, the higher is the dispersion, or the smaller is the particle size.

The surfaces of the as-received materials are covered by O and/or OH species, as indicated by the peak at 1.098 G kHz^{-1}. Remarkably, these surfaces were effectively cleaned simply by holding the electrode potential within the electrochemical double-layer region. This mild surface-reduction procedure should be contrasted to the rigorous and often technically demanding methods employed at the solid–gas interface, which usually involve several cycles of high-temperature calcination and reduction, limiting the choice of catalyst support to, typically, nonconductive oxides such as alumina, titania, and silica.

However, extensive potential cycling, which is a widely used in electrode-surface cleaning procedure, sinters the nanoscale electrocatalyst. Although the sample in Fig. 4(c) started with the same as-received electrocatalyst as that shown in Fig. 4(b), the dispersion estimated from the corresponding ^{195}Pt NMR spectrum is only about 27% [30], far lower than the 50% obtained from Fig. 4(b). This dispersion lowering provides clear evidence for sintering produced by potential cycling, an effect that clearly needs to be borne in mind when analyzing the results of both ligand and metal EC-NMR experiments.

3.1.3.2 Correlation between the Knight Shift of a Platinum Surface and the Electronegativity of the Adsorbate

Understanding how adsorbates modify the chemical and physical properties of metal surfaces has long been one of the central themes of surface science, and is of importance in relation to the ability to scientifically engineer metal surface properties for targeted applications, such as enhancing the CO tolerance of electrocatalysts used in fuel cells, or more generally in promoting metal surface catalysis. As demonstrated in Sect. 3.1.3.1, interfacial electrochemistry offers an elegant way to modify electrode surfaces while ^{195}Pt NMR provides a powerful probe to follow the variations in the physical properties of metal surfaces caused by such modifications. By using this strategy, the influence of a series of different ligands (H, O, S, CN^-, CO, and Ru), electrochemically adsorbed onto carbon-supported nanoscale Pt particles from the same starting batch, has been investigated by ^{195}Pt NMR, in an electrochemical environment [10].

The starting electrode material used for this series of experiments was the same as that used in the previous section. As shown there, the frequency difference between the resonance positions of surface and bulk platinum atoms at 8.5 T is about 2.5 MHz, large enough to provide a very convenient spectral visualization of how deep the influence of an adsorbate can go, as illustrated by the point-by-point ^{195}Pt NMR spectra (recorded at 80 K) presented in Fig. 5. These spectra are normalized by equalizing their amplitudes

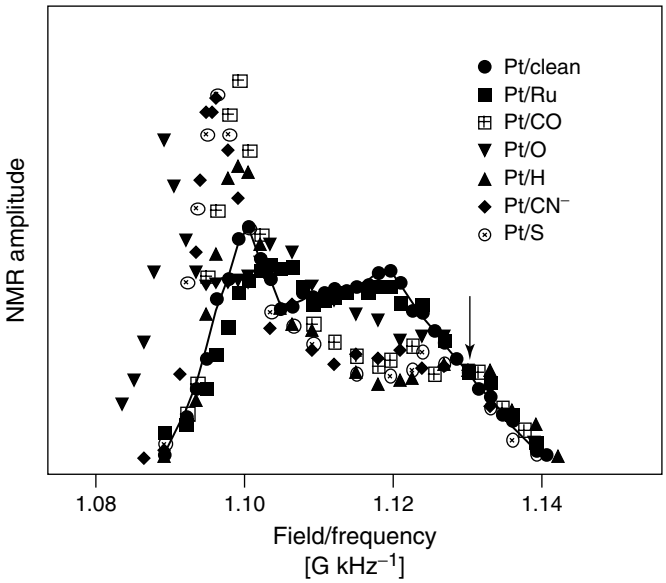

Fig. 5 Superimposition of point-by-point, 8.47 T ^{195}Pt NMR spectra of a 2.5 nm, carbon-supported Pt electrocatalyst without and with different chemisorbed ligand: Ru, CO, O, H, CN^-, and S. The spectra were normalized by equalizing the amplitude at 1.131 G kHz^{-1} (indicated by the arrow). The invariance of signals beyond 1.131 G kHz^{-1} provides experimental confirmation of the Friedel–Heine invariance theorem. The surface peaks range over ~11 000 ppm. (Reproduced with permission from Ref. [10], Copyright by © 2000 American Chemical Society.)

at 1.131 G kHz^{-1}, which is indicated by the arrow. The interesting observation here is that the position of the high-field signal intensity (above 1.131 G kHz^{-1}), which is due to Pt atoms within the three innermost layers, is independent of adsorbate type. This independence provides direct experimental evidence for the validity of the Friedel–Heine invariance theorem [32, 33], which states that the integral electronic properties at an atom, such as its LDOS, are determined primarily by the surrounding medium, within a few electronic wavelengths. This is exactly what is observed – although the chemical identity of the adsorbates is quite varied, their influences, to a very good approximation, do not go beyond their next-nearest neighbors. That is, the high-field signals are invariant towards "boundary" changes.

In complete contrast to the Friedel–Heine invariance of the electronic properties observed for the innermost platinum particle layers, the surface and subsurface NMR signals undergo major frequency shifts as different chemical species are adsorbed, as can be seen in Fig. 5. The NMR layer-model spectral deconvolution [31] technique was applied to these spectra in order to obtain the variations in the surface and subsurface Knight shifts. Because of the Friedel–Heine invariance, the NMR parameters (peak

position, width, relative intensity) for the three central layers were fixed to the clean-surface values, while the surface and subsurface peak positions were allowed to vary. For Pt/O, the position of the third layer was also varied, as a result of the long healing length in this system, plus the surface peak areas were also varied in some simulations, as a result of saturation effects caused by longer T_1 values. The results of these simulations are shown in Fig. 6 and the surface and subsurface peak shift values obtained are plotted in Fig. 7 as a function of the Allred–Rochow electronegativity (defined as the electrostatic force exerted by the nucleus of the atom on its valence electrons) of the bonded adsorbate atom. Remarkably, both the surface and subsurface peak positions map almost linearly the electronegativity of the adsorbate. The reasons for this are as follows:

According to the layer model, Eq. (4), one has $K_1 = K_\infty + (K_0 - K_\infty)\exp(-1/m)$ for the subsurface layer, $n = 1$. A simple mathematical conversion gives $m = 1/\ln[(K_0 - K_\infty)/(K_1 - K_\infty)]$. By replacing K_1 and K_0 by the correlation lines shown in Fig. 7,

$$K_0(\text{ppm}) = (-10.2 + 5.3\chi) \times 10^3 \quad (5)$$

$$K_1(\text{ppm}) = (-21.5 + 5.8\chi) \times 10^3 \quad (6)$$

m (the healing length) can then be directly expressed as a function of the electronegativity χ:

$$m = \frac{1}{\ln}\left[\frac{(23.2 + 5.3\chi)}{(11.9 + 5.8\chi)}\right] \quad (7)$$

In Fig. 8, the healing length ($= 0.229\,m$, where 0.229 nm is the layer thickness for Pt particles) is plotted as a function of the electronegativity, Eq. (7). This result shows that the larger the electronegativity of the adsorbate, the longer the healing length, that is, the deeper the influence of the adsorbate goes. It is also interesting to note that the value of the healing length m for hydrogen ($\chi = 2.2$) adsorption obtained via Eq. (7) is about 2.9, which is very close to the $m = 2.6$ value found

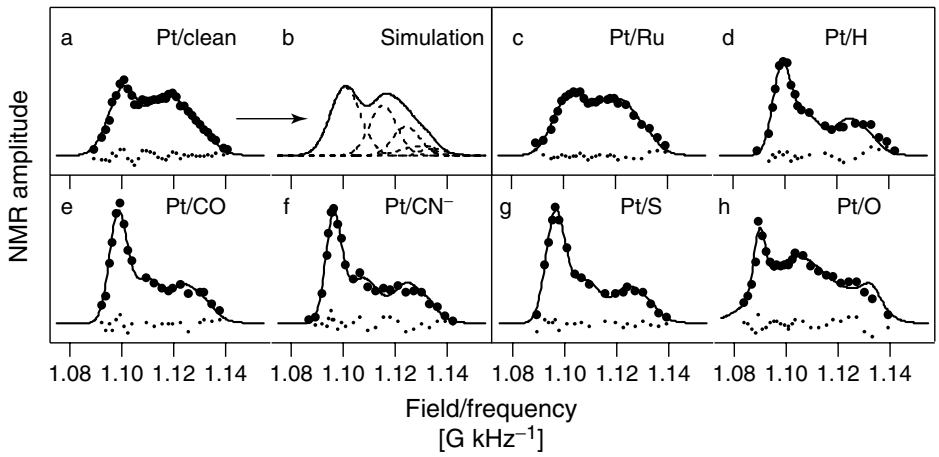

Fig. 6 The NMR layer-model simulations of the ^{195}Pt spectra shown in Fig. 5 and the small dots are the variances between the experimental and fitted values. (a) clean-surface Pt; (b) Simulation of (a); (c) Pt with adsorbed Ru; (d) Pt with adsorbed H; (e) Pt with adsorbed CO; (f) Pt with adsorbed cyanide; (g) Pt with adsorbed S (from Na_2S solution); (h) Pt with adsorbed O. (Reproduced with permission from Ref. [10], Copyright by American Chemical Society 2000.)

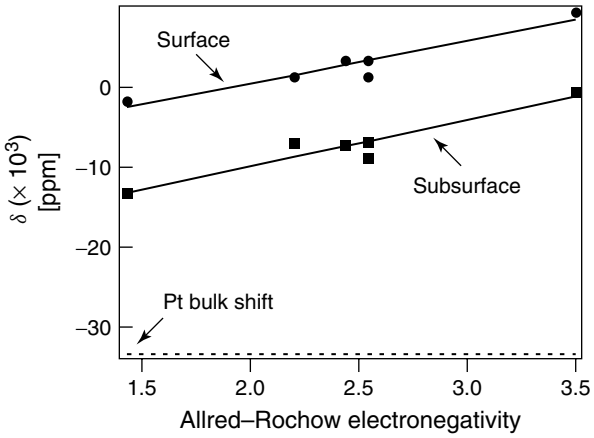

Fig. 7 Correlation between surface/subsurface frequency shifts (with respect to the Pt NMR reference H_2PtCl_6) and the Allred–Rochow electronegativity. The dashed horizontal line indicates the Knight shift of bulk platinum atoms. The solid straight lines are linear fits to the surface and subsurface shifts as a function of the electronegativity. Both have R^2 values of ca. 0.92. (Reproduced with permission from Ref. [10], Copyright by American Chemical Society 2000.)

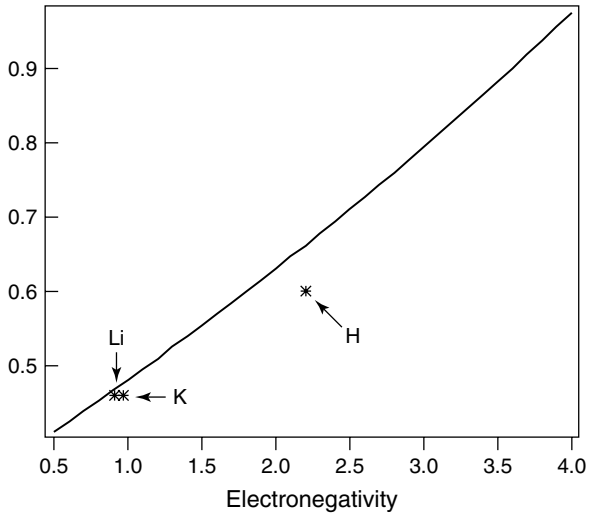

Fig. 8 Solid curve showing the relationship between the healing length and electronegativity as determined from Eq. (7). For comparison, we also show the three experimental points based on previous observations. See the text for details. (Reproduced with permission from Ref. [10], © Copyright by American Chemical Society 2000.)

by a detailed layer-model analysis [31]. In addition, for the adsorption of the alkali metal elements ($\chi \sim 1$), Eq. (7) predicts $m \sim 2$, virtually the same m as obtained for clean-surface Pt particles in an electrochemical environment. One would, therefore, expect that alkali adsorption would not significantly change the ^{195}Pt NMR spectrum of small Pt particles after adsorption. This is exactly what has been observed experimentally (in a gas-phase system) [34]. For comparison, these three experimentally estimated points are also plotted in Fig. 8.

The invariance of the frequency shifts of the more buried (deeper than the third layer) Pt atoms to surface adsorbate electronegativity provides strong evidence demonstrating the applicability of Friedel–Heine invariance of the E_F-LDOS in these nanoscale electrocatalyst systems. This is a rather interesting extension of the original Friedel–Heine invariance theorem to nanoscale systems and may have utility in describing the electronic surface structure of metal catalysts in different chemical environments. These results may also be expected to lead to useful general correlations between electronic properties and more conventional chemical descriptors (such as ligand electronegativity), which could be helpful in understanding the electronic structure of metal–adsorbate interfaces by providing guidelines for engineering new electrode surfaces.

3.1.3.3 Correlation between the Clean-surface E_F-LDOS of Metals and the Knight Shift of Adsorbates

Because NMR has elemental specificity and is also nondestructive, it offers unique opportunities for investigating electrochemical problems from both sides of the electrochemical interface. This strategy has been applied to investigate the metal–CO interactions in a number of recent studies [25].

The discussions in the two previous sections demonstrate that there is an unambiguous NMR discrimination between the surface peak (at 1.100 G kHz^{-1} for nanoscale platinum particles) and the rest of the platinum sites. By carrying out detailed temperature-dependent T_1 relaxation measurements on a given Pt sample, a value for $S(T_1T)^{-1}$ can be obtained, and by using the two-band model (see Sect. 3.1.2.1), a pair of surface Pt s- and d-$D(E_F)$s can therefore be deduced. Similarly, $S(T_1T)^{-1}$ and K measurements on ^{13}CO adsorbed onto the metal surfaces can give the corresponding ^{13}C 5σ and $2\pi^*$ (E_F)s (see Sect. 3.1.3.4).

It is of fundamental interest to see if there exists any type of correlation between the clean-surface E_F-LDOS of the metal and the ^{13}C Knight shift of the chemisorbed CO. The former is an important surface attribute defining the ability of the metal surface to donate (to act as a HOMO) as well as to accept (to act as a LUMO) electrons, while the latter measures, at least to a certain extent, the degree of metallization of chemisorbed CO (see Sect. 3.1.3.4). We show in Table 1, a set of data for atop CO on Pt and Pd, shown graphically in Fig. 9. The purely orbital contributions (chemical shifts) for atop CO on Pt and on Pd were calculated by using density functional theory (DFT) calculations on model $COPt_7$ and $COPd_7$ clusters in which CO sits atop the central metal atom, which is coordinated by the remaining six metal atoms. For $COPt_7$, a value of 160 ± 20 ppm from tetramethylsilane (TMS) was obtained, while for $COPd_7$, the value was 203 ± 20 ppm. These calculated values are in good agreement with available experimental data

Tab. 1 Correlation between clean-surface E_F-LDOS and ^{13}C shift of chemisorbed CO [25]. The Knight shift = total shift − chemical shift

Sample	*Clean-surface E_F-LDOS (Ry^{-1} $atom^{-1}$)*	*Total ^{13}C shift of $CO_{chemisorbed}$ (ppm w.r.t TMS)*
$PtCO_7$	0	160
CO–Pt/oxides (dry)	14.8	330
CO–Pt/carbon (wet)	17.7[a]	351[a]
CO–Pt/carbon (wet)	18.6	383
$PdCO_7$	0	203
CO–Pd/oxides (dry)	24	500

[a]For an 8.8-nm sample.

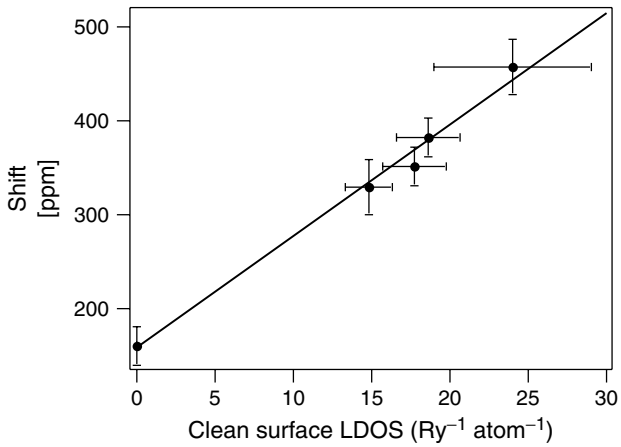

Fig. 9 Correlation between the Fermi level total electronic densities of states at transition metal (Pt and Pd) surfaces (in Ry^{-1} $atom^{-1}$) and the corresponding ^{13}C Knight shift of chemisorbed CO. (Partially reproduced with permission from Ref. [25], © Copyright by American Chemical Society.)

while the standard deviations account for uncertainties caused by the use of different functionals and basis sets. The clean-surface E_F-LDOS for Pd was estimated on the basis of the changes in magnetic susceptibility of small Pd particles with respect to their bulk value, by application of the exponential healing model.

As shown in Fig. 9, the ^{13}C NMR shift of CO responds linearly to the clean-surface E_F-LDOS before adsorption. The straight line is a linear fit to the data, giving a slope of 12 ppm/Ry^{-1} $atom^{-1}$. This linear relationship can be readily related to the frontier orbital interpretation of the Blyholder model [35] – a higher clean-surface E_F-LDOS means more metal electrons and holes are available to engage in 5σ-forward and $2\pi^*$-back donation. As the E_F-LDOS increases, CO becomes more metallic, which results in a larger

Knight shift. A correlation very similar in nature to this has also been found to exist in the "gas phase", in which the C–O vibrational stretch frequency (after chemisorption) was shown to correlate linearly with the Pt clean-surface E_F-LDOS before chemisorption [36]. The higher the surface E_F-LDOS, the lower the C–O stretching frequency.

The linear relationship shown in Fig. 9 is important because it demonstrates the validity of the frontier orbital interaction picture of metal surface chemistry, in which the importance of the clean-surface E_F-LDOS is highlighted. In addition, it puts ^{13}C NMR spectroscopy of chemisorbed CO on a firmer footing, by probing the electronic properties of transition metal surfaces *before* CO chemisorption.

3.1.3.4 Coupling EC-NMR with In Situ Infrared Spectroelectrochemistry

It is now clear that CO acquires metallic properties upon adsorption onto transition metal surfaces, as indicated by the presence of a Knight shift and a Korringa relationship, measured via ^{13}C NMR. Furthermore, by using the experimentally measured ^{13}C Knight shift and the Korringa constant, a phenomenological two-band model [10] permits a quantitative partitioning between the 5σ- and $2\pi^*$-$D(E_F)$ at ^{13}C to be obtained, providing insight into metal–CO bonding at the electronic level. These types of ^{13}C NMR study have been carried out on ^{13}CO chemisorbed (ex MeOH) onto a series of carbon-supported, fuel cell grade, commercial platinum electrocatalysts having different average particle size: 2.0, 2.5, 3.2, 3.9, and 8.8 nm, in which both metal and adsorbation E_F-LDOS might be expected to vary with particle size. Shown in Fig. 10 is a typical ^{13}C NMR spectrum and temperature-dependent T_1 data for the 8.8-nm sample [10]. The straight line through the origin is characteristic of the Korringa relationship, indicating the metallic state of adsorbed CO in this electrocatalyst system.

Table 2 collects all of the ^{13}C NMR results together with values of the 5σ- and $2\pi^*$-$D(E_F)$ deduced from these results, in addition to the corresponding infrared data [37] (vide infra). The results shown in Table 2 indicate that the major part of the total E_F-LDOS at ^{13}C is from the $2\pi^*$-like electrons, with $2\pi^*$-$D(E_F)$ being about 10 times larger than the $5\sigma - D(E_F)$. These values are in good agreement with theoretical band structure calculations. The contribution to the spin–lattice relaxation rate ($1/T_1$) is dominated by orbital and dipolar interactions, consistent with the dominance of π-like electrons at the Fermi level. Notice that while $5\sigma - D(E_F)$ is almost a constant, the $2\pi^*$-$D(E_F)$ varies noticeably from sample to sample. However, since NMR only measures the electron density at a given energy level, that is, the Fermi level, it does not provide complete information about the total electron densities for forward-

Tab. 2 The 5σ- and $2\pi^*$-$D(E_F)$s deduced by the two-band model from ^{13}C NMR data of CO chemisorbed on Pt electrocatalysts [10] and the corresponding SNIFTIRS C–O vibrational stretching frequencies [37]

Size (nm)	*5σ-$D(E_F)$ (Ry molecule)$^{-1}$*	*$2\pi^*$-$D(E_F)$ (Ry molecule)$^{-1}$*	*IR frequency (cm)$^{-1}$*
8.8	0.6	6.4	2044
3.9	0.6	6.6	2043
3.2	0.6	6.5	2044
2.5	0.7	6.8	2038
2.0	0.6	7.3	2028

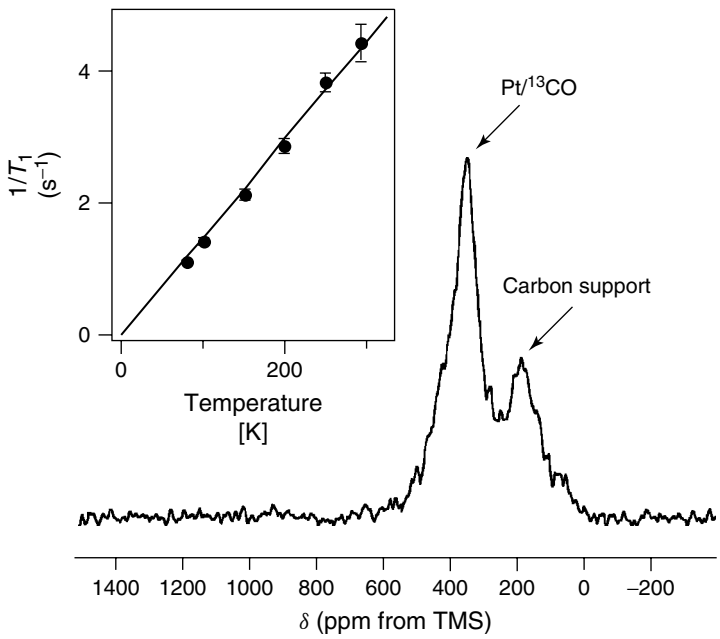

Fig. 10 A typical ^{13}C NMR spectrum and temperature-dependent T_1 data for an 8.8-nm Pt/C sample. The straight line through the origin is characteristic of the Korringa relationship, indicating the metallic state of adsorbed CO in this electrocatalyst system. (Adapted from Ref. [10].)

and backdonation, which are the integrals of the LDOS from the bottom of the conduction band to the Fermi level. Nevertheless, as can be seen in Table 2, the variation in the total E_F-LDOS between different samples are mainly due to changes in the $2\pi^*$-$D(E_F)$. This suggests that the changes in chemical properties of adsorbed CO are mainly determined by variations in backbonding. In particular, if the Fermi level cuts the tail of the $2\pi^*$ band as it rises, then the increase in the $2\pi^*$-$D(E_F)$ would indicate an enhancement in backdonation, and a decrease in the corresponding vibrational C–O stretch frequency.

In situ subtractively normalized interfacial Fourier transform infrared reflectance spectroelectrochemistry (SNIFTIRS) studies confirm this prediction [37]. They also yield a linear correlation between ν_{CO} and the $2\pi^*$-$D(E_F)$, Table 2, with a slope of $-19 \pm 2\ \mathrm{cm}^{-1}/(\mathrm{Ry\ molecule})^{-1}$ and an intercept of $2167 \pm 20\ \mathrm{cm}^{-1}$, as shown in Fig. 11. The latter value is quite close to the value expected for free CO, $\nu = 2143\ \mathrm{cm}^{-1}$. On the basis of these results, the following overall physical picture of carbon monoxide adsorbed onto a platinum electrode can be proposed: Since the 5σ orbital of CO is essentially nonbonding, with the lone pair concentrated on carbon and the $2\pi^*$ orbital is a much less polarized antibonding orbital, the change in CO stretch frequency is mainly governed by changes in $2\pi^*$ backdonation: the higher the backdonation, the lower the CO stretch frequency.

The above example demonstrates the complementary nature of in situ infrared

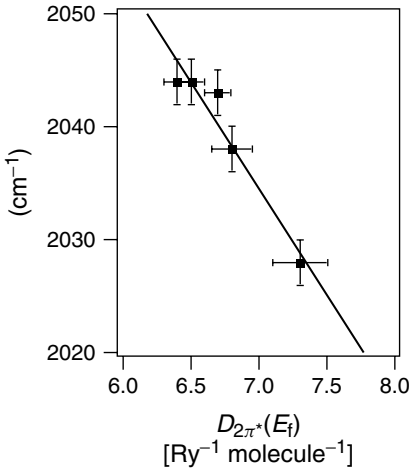

Fig. 11 Correlations between ν_{CO} and $2\pi^*$-$D(E_F)$. The straight line is the linear fit that gives a slope of -19 cm^{-1}/Ry^{-1} molecule^{-1} and an intercept of 2167 cm^{-1}, with a $R^2 = 0.98$. (Part of the results shown in this figure has been published in Refs. [10, 37].)

spectroscopy and solid-state NMR, in providing insights into the details of surface chemistry of electro-chemisorbed CO on platinum. While SNIFTIRS – a major research technique of the interfacial electrochemical community – provides important qualitative information regarding the bond strengths of adsorbed CO, it offers somewhat less insight into the electronic relocations that occur within the bond, the electron distribution as a function of sample composition and morphological detail. For instance, how the bond changes as a function of particle size is difficult to learn using infrared alone. However, a ^{13}C NMR analysis of the 5σ- and $2\pi^*$-E_F-LDOS at the carbon atom offers a quantitative description of metal–CO bonding in terms of changes in the E_F-LDOS. The joint SNIFTIRS/NMR approach provides new information on the electronic structure of the metal–solution interface, which is relevant to the characterization of industrial fuel cell catalysts, as well as other interfacial electrochemical systems of practical importance, by combining bond strength (IR) and quantitative E_F-LDOS results (NMR).

3.1.3.5 Surface Diffusion

The rationale behind using NMR to study surface diffusion is that the correlation time for diffusion, τ, can be related to the temperature dependence of the NMR relaxation rates observed for diffusing atoms or molecules [12]. Under certain circumstances, such a relation can be expressed analytically, permitting a quantitative analysis of the data in dynamic and thermodynamic terms.

When using the temperature dependence of the nuclear spin–spin or nuclear spin–lattice relaxation rate to study molecular motion, as is the case with the surface diffusion we are dealing with here, there exist so-called "strong" and "weak" collision limits. Different mathematical relationships are needed to describe these limits. Consider the nuclear spin–spin relaxation rate ($1/T_2$) as measured by a conventional Hahn-echo pulse sequence, and suppose that $\Delta\omega$ is the amplitude of the local field fluctuation responsible for relaxation. Also assume that τ is the correlation time for the motion, say a jump, which causes the local field to fluctuate. The strong collision limit is defined such that

$\tau \gg 1/\Delta\omega$. At $t = 0$, that is, just after the first $\pi/2$ pulse, which flips all nuclear spins into the xy plane, all spins are in phase, and they retain their phase memory until $t = \tau$, when the collision changes the direction of the local field. Since τ is sufficiently long to dephase the spins, they lose all phase memory before the next collision. Therefore, $1/T_2 = 1/\tau$. In contrast, in the weak collision limit, $\tau \ll 1/\Delta\omega$. Since τ is relatively short, insufficient dephasing builds up between two consecutive jumps. When the spin jumps randomly, many jumps are needed in order to accumulate sufficient dephasing, and one has $1/T_2 = (\Delta\omega)^2\tau$. In summary then, we have for these two limiting cases:

$$\frac{1}{T_2} = \frac{1}{\tau} \text{ for } \tau \gg \frac{1}{\Delta\omega} \tag{8}$$

and

$$\frac{1}{T_2} = (\Delta\omega)^2\tau \text{ for } \tau \ll \frac{1}{\Delta\omega} \tag{9}$$

Fortunately, the function

$$\frac{1}{T_2} = \frac{(\Delta\omega)^2\tau}{(1 + (\Delta\omega)^2\tau^2)} \tag{10}$$

satisfies both limiting cases. In fact, Eq. (10) is similar to the typical spectral density function used for a randomly fluctuating local field at a frequency $\Delta\omega$, and as we show below, the use of these simple relations leads to information on both the rates of surface diffusion and the associated energetics.

The temperature dependence of $1/T_2$ for ^{13}CN (a) [6] and for ^{13}CO (b) [5] on polycrystalline platinum black at saturation coverage are shown in Fig. 12. For CO or CN adsorbed onto small platinum particles, $1/T_2$ can be expressed as

$$\begin{aligned}\frac{1}{T_2} &= \frac{1}{T_2{}^{\mathrm{RL}}} + \frac{1}{T_2{}^{\mathrm{Pt}}} + \frac{1}{T_2{}^{\mathrm{dip}}} + \frac{1}{T_2{}^{\mathrm{diff}}} \\ &= \frac{1}{T_2{}^{\mathrm{RL}}} + aT + \frac{(\Delta\omega)^2\tau}{(1+(\Delta\omega)^2\tau^2)} + \frac{1}{(N\tau)}\end{aligned} \tag{11}$$

where $1/T_2{}^{\mathrm{RL}}$ is the temperature-independent "rigid lattice" contribution, and $1/T_2{}^{\mathrm{Pt}}(= aT$, where a is a constant and T the absolute temperature) accounts for the effects of platinum spins. $1/T_2{}^{\mathrm{dip}} = (\Delta\omega)^2\tau/(1 + (\Delta\omega)^2\tau^2)$, where $\Delta\omega$ is the dipolar field in Hertz and $\tau = \tau_0 \exp(E/k_{\mathrm{B}}T)$, with τ_0 a preexponential factor, chosen to be 10^{-13} s, and E is the activation energy for surface diffusion), arises from dipolar interactions between neighboring carbon- 13 spins. $1/T_2{}^{\mathrm{diff}}(= 1/N\tau$, where N is the number of jumps needed to dephase the carbon spins) comes from the field difference (positive or negative) between adjacent adsorption sites, due to the presence of a significant magnetic field inhomogeneity on the particle surface.

The solid lines in Fig. 12 are the fit to Eq. (11) with $1/T_2{}^{\mathrm{RL}}$, a, $\Delta\omega$, E, and N as fitting parameters. The results of the fits (in which $1/T_2{}^{\mathrm{RL}}$ are 293 and 930 s^{-1} for CO and CN, respectively) are also shown in Fig. 12. Clearly, this simple model describes the experimental data very well, for both ^{13}CO and ^{13}CN. It is interesting to note that the activation energy found for CO (7.8 kcal mol^{-1}) is close to that found for CO on "dry" alumina-supported Pt clusters, as well as that found in single-crystal studies. The results of the fits also indicate that the activation energy for surface diffusion is higher for CN than for CO, while the difference in the constant a suggests, paradoxically, that platinum has more of an electronic influence on ^{13}C

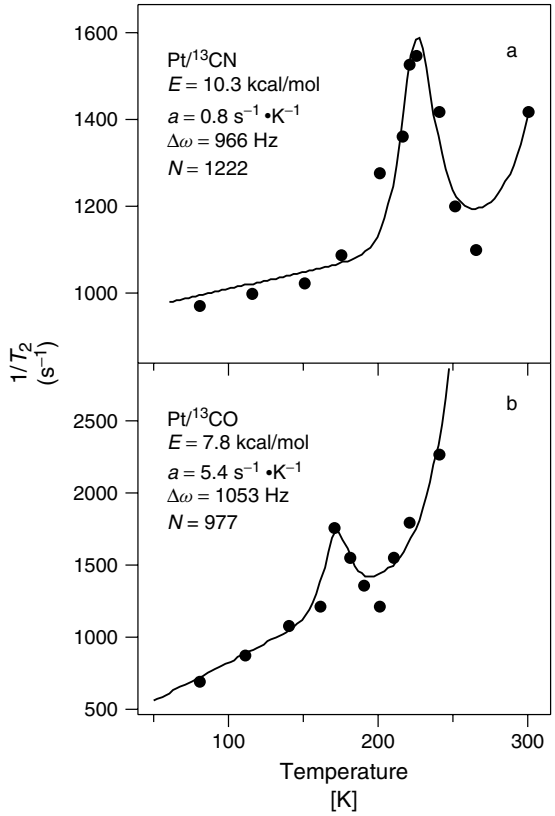

Fig. 12 Temperature dependence of spin–spin relaxation rates of chemisorbed and (panel a) ^{13}CN and (panel b) ^{13}CO on 10-nm Pt electrocatalyst surfaces. The solid lines are the fits to Eq. (11) and the numbers are the corresponding results of the fits. (Adapted from Refs. [5, 6].)

spin–spin relaxation of CO than on that of CN. The latter may, however, be related to the fact that the J-coupling is mediated by orbital electrons between ^{13}C and ^{195}Pt and is expected to be primarily influenced via σ-bonding rather than through π-bonding, for $|\psi|^2 = 0$ at C for the $2\pi^*$ orbital. If the ^{195}Pt–^{13}C dipolar interaction were the only mechanism for $1/T_2{}^{\mathrm{Pt}}$, the ratio in a values would yield $r_{\mathrm{Pt-CN}}/r_{\mathrm{Pt-CO}}$ equal to 1.9, which is unrealistic. Thus, while the activation values may indicate an overall stronger metal surface bonding for Pt–CN than for Pt–CO, the a values suggest that σ-bonding is stronger in the latter case. Finally, $\Delta\omega$ for the ^{13}C–^{13}C dipolar interaction is essentially identical in each of the systems investigated, consistent with a similar adsorbate coverage for both samples.

3.1.3.6 Isotopic Labeling for Site Selectivity

Isotopic labeling is a very useful and geometrically specific NMR technique when the natural abundance of the nucleus of interest is too low to be detected under normal conditions, such as with ^{13}C, ^{15}N, and ^{17}O. As an example, we consider here the bonding of a larger species, acetonitrile, bonded to Pt in an electrochemical environment [40]. ^{13}C $1/T_1$ versus T data for $CH_3{}^{13}CN$ and $^{13}CH_3CN$ adsorbed on platinum are shown in Fig. 13. A linear $1/T_1$ versus T plot, reflecting Korringa behavior with

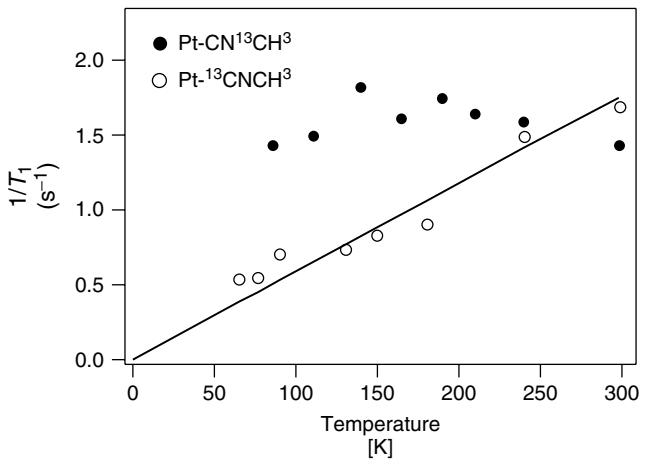

Fig. 13 Temperature dependence of spin–lattice relaxation rates for chemisorbed $CH_3{}^{13}CN$ and $^{13}CH_3CN$. The clear absence of a Korringa relationship for $^{13}CH_3CN$ (solid circles) indicates that the carbon atom in the methyl group does not acquire any metallic character. (Adapted from Ref. [38].)

$T_1T = 170$ s K, is only obtained with the $CH_3{}^{13}CN$ adsorbate. This proves that at least the carbon of the CN group is directly attached to platinum, and that the ^{13}C has acquired metallic character. Note that the value of $T_1T = 170$ s K for $CH_3{}^{13}CN$ is quite close to that of ^{13}CN (135 s K). The T_1T product for ^{15}N in $CH_3C^{15}N$ at room temperature is 224 s K, showing that the spin–lattice relaxation of ^{15}N in chemisorbed $CH_3C^{15}N$ is much more efficient than in chemisorbed $C^{15}N$, where T_1T varied in the range ~3000–4000 s K. Indeed, after taking into account the $\gamma_{13C}/\gamma_{15N} \sim 2.5$ factor in Eq. (3), the relaxation of ^{15}N appears even more efficient than that of the "metallic" ^{13}C in $CH_3{}^{13}CN$. This suggests that both C and N in the CN group are directly attached to the platinum surface, forming a side-on parallel orientation with respect to the Pt–Pt surface bonds. The clear absence of a Korringa relationship for $^{13}CH_3CN$ (solid circles) indicates that the carbon atom in the methyl group does not acquire any metallic character. This implies that neither C–C bonding nor antibonding orbitals are involved with bonding to the platinum surface, while both ^{13}C and ^{15}N atoms in the CN group are strongly involved, in contrast to the situation with the CN itself, in which cyanide has a C-down on-top bonding.

3.1.3.7 Potential-dependent EC-NMR

Understanding the nature of the electric field (electrode potential) effects on the electronic structure at the solid–liquid interface is an outstanding issue in electrocatalysis and in the theory of the electrical double layer. To illustrate such effects via NMR, we show in Fig. 14, the electrode potential–induced ^{13}C line shifts for CO (circles) [8] and CN (squares) [6] on polycrystalline Pt. These results were obtained under active external potentiostatic control, and at room temperature, and the inset shows typical ^{13}C NMR spectra of ^{13}CN, recorded at

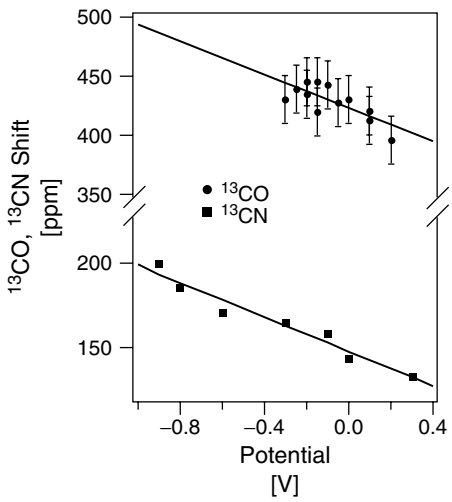

Fig. 14 Electrostatic potential dependence of ^{13}C shifts for ^{13}CO (circles) and ^{13}CN (squares) chemisorbed on a 10-nm Pt electrocatalyst. (Adapted from Ref. [4].)

different applied potentials. Apparently, for both adsorbates, there is a linear relation between the electrode potential and the line shift – the more negative the potential, the larger the frequency shift. ^{13}C becomes more deshielded as the potential goes to more negative values, and the slope is about -71 ppm V^{-1} for ^{13}CO and -50 ppm V^{-1} for ^{13}CN. For CO on Pd, the slope was found to be even larger, that is, about -136 ppm V^{-1} [8].

A similar response in C–O vibrational frequency, ν_{CO}, to variations in the electrode potential has been reported [39]. There, ν_{CO} decreased when the electrode potential became more cathodic. However, the origin of this so-called vibrational Stark effect has been controversial for some time, since a clear picture of how the short-range (electronic) bonding and the longer-range (electrostatic) field effects at surfaces are controlled by varying either the electrode or the surface potential, has not been available.

EC-NMR provides an additional technique with which to probe these questions, for several reasons. First, the response of ^{13}C NMR to the electrode potential has been found to be due essentially to the Knight shift [8]. The ^{13}C chemical shift response of CO to electric fields (in biomolecules) has been estimated to be at most about -15 ppm V^{-1}, much smaller than the values found at the electrochemical interface (see above). In addition, for CO on Pd, a corresponding change in the nuclear spin–lattice relaxation rate as a function of applied field has also been observed [8], indicating the electronic nature of the change in NMR shift. Second, the magnitude of the clean-surface E_F-LDOS of the adsorbent is responsible for the extent of the Knight shift as well as the vibrational stretch frequency of chemisorbed CO [25, 36]. That is to say, the higher the clean-surface E_F-LDOS, the larger (lower) will be the ^{13}C Knight shift [25] (C–O stretch frequency [36]) of CO, after chemisorption. Both relationships are linear, with slopes of about 12 ppm/Ry^{-1}·$atom^{-1}$ and -4 cm^{-1}/Ry^{-1}·$atom^{-1}$, respectively, giving a ratio of -3 ppm/cm^{-1}. This is to be compared with the ratio of -2.8 ppm/cm^{-1}, obtained independently

from the slopes (-71 ppm V^{-1} and 25 cm^{-1} V^{-1}, respectively) of $\delta(^{13}C)$ and ν_{CO} versus electrode potential relationships for CO on Pt black. Third, as shown in Sect. 3.1.3.4, variations in ν_{CO} can be directly correlated with changes in $2\pi^*$ backdonation – that is, the higher the backdonation, the lower the CO stretch frequency. When taken together, all these observations indicate that the potential dependence of both the ^{13}C NMR shift and the vibrational stretch frequency of adsorbed CO are primarily electronic in nature, and originate from changes in the E_F-LDOS at the metal surface and at the adsorbate, induced by electrode polarization.

3.1.4
Future Perspectives

EC-NMR has made considerable progress during the past few years. It is now possible to investigate in detail metal–liquid interfaces under potential control, to deduce electronic properties of electrodes (platinum) and of adsorbates (CO), and to study the surface diffusion of adsorbates. The method can also provide information on the dispersion of commercial carbon-supported platinum fuel cell electrocatalysts and on electrochemically generated sintering effects. Such progress has opened up many new research opportunities since we are now in the position to harness the wealth of electronic, E_F-LDOS as well as dynamic and thermodynamic information that can be obtained from NMR experiments. As such, it is to be expected that EC-NMR will continue to thrive and may eventually become a major characterization technique in the field of interfacial electrochemistry.

Acknowledgments

This work was supported by the United States National Science Foundation (grant CTS 97-26419), by an equipment grant from the United States Defense Advanced Research Projects Agency (grant DAAH 04-95-1-0581), and by the US Department of Energy under grant DEFG02-96ER45439.

References

1. A. Zangwill, *Physics at Surfaces*, Cambridge University Press, Cambridge, 1988.
2. G. A. Somorjai, *Introduction to Surface Chemistry and Catalysis*, John Wiley & Sons, New York, 1994.
3. A. Wieckowski, (Ed.), *Interfacial Electrochemistry – Theory, Experiment, and Applications*, Marcel Dekker, New York, 1999.
4. Y. Y. Tong, E. Oldfield, A. Wieckowski, *Anal. Chem.* **1998**, *70*, 518A–527A.
5. J. B. Day, P.-A. Vuissoz, E. Oldfield et al., *J. Am. Chem. Soc.* **1996**, *118*, 13 046–13 050.
6. J. J. Wu, J. B. Day, K. Franaszczuk et al., *J. Chem. Soc., Faraday Trans.* **1997**, *93*, 1017–1026.
7. Y. Y. Tong, C. Belrose, A. Wieckowski et al., *J. Am. Chem. Soc.* **1997**, *119*, 11 709, 11 710.
8. P.-A. Vuissoz, J.-P. Ansermet, A. Wieckowski, *Phys. Rev. Lett.* **1999**, *83*, 2457–2460.
9. Y. Y. Tong, C. Rice, E. Oldfield et al. in *Theoretical Modeling of the Solid/Liquid Interface: Electronic Perspective and Comparison with Experiment* (Ed.: W. Halley), American Chemical Society, Washington, DC, 2001.
10. Y. Y. Tong, C. Rice, A. Wieckowski et al., *J. Am. Chem. Soc.* **2000**, *122*, 1123–1129, 11 921–11 924.
11. M. E. Lacey, R. Subramanian, D. L. Olson et al., *Chem. Rev.* **1999**, *99*, 3133–3152.
12. C. P. Slichter, *Principles of Magnetic Resonance*, 3rd Enlarged and Updated Edition, Springer-Verlag, Berlin, Germany, 1990.
13. J.-P. Ansermet, C. P. Slichter, J. H. Sinfelt, *Prog. NMR Spectrosc.* **1990**, *22*, 401–421.
14. T. M. Duncan, *Colloids Surf.* **1990**, *49*, 11–31.
15. M. Pruski in *Encyclopedia of Magnetic Resonance* (Eds.: D. M. Grant, R. K. Harris),

John Wiley & Sons, New York, 1996, pp. 4638–4638, Vol. 7.
16. J. J. van der Klink, *Adv. Catal.* **2000**, *44*, 1–117.
17. P.-K. Wang, J.-P. Ansermet, S. L. Rudaz et al., *Science* **1986**, *234*, 35–41.
18. P. J. Slezak, A. Wieckowski, *J. Magn. Reson., Ser. A* **1993**, *102*, 166–172.
19. W. D. Knight in *Solid State Physics* (Eds.: F. Seitz, D. Turnbull), Academic Press, New York, 1956, pp. 93–136, Vol. 2.
20. J. J. van der Klink, H. B. Brom, *Prog. NMR Spectrosc.* **2000**, *36*, 89–201.
21. J. Korringa, *Physica* **1950**, *16*, 601–610.
22. J.-P. Bucher, J. J. van der Klink, *Phys. Rev. B* **1988**, *38*, 11 038–11 047.
23. R. Hoffmann, *Rev. Mod. Phys.* **1988**, *60*, 601–628.
24. P.-A. Vuissoz, J.-P. Ansermet, A. Wieckowski, *Electrochim. Acta* **1998**, *44*, 2457–2460.
25. Y. Y. Tong, C. Rice, N. Godbout et al., *J. Am. Chem. Soc.* **1999**, *121*, 2996–3003.
26. M. S. Yahnke, B. M. Rush, J. A. Reimer et al., *J. Am. Chem. Soc.* **1996**, *118*, 12 250, 12 251.
27. B. M. Rush, J. A. Reimer, E. J. Cairns, *J. Electrochem. Soc.* **2001**, *148*, A137–A148.
28. H. E. Rhodes, P.-K. Wang, H. T. Stokes et al., *Phys. Rev. B* **1982**, *26*, 3559–3568.
29. J. J. van der Klink, J. Buttet, M. Graetzel, *Phys. Rev. B* **1984**, *29*, 6352–6355.
30. C. Rice, Y. Y. Tong, E. Oldfield et al., *Electrochim. Acta* **1998**, *43*, 2825–2830.
31. J. P. Bucher, J. Buttet, J. J. van der Klink et al., *Surf. Sci.* **1989**, *214*, 347–357.
32. J. Friedel, *Adv. Phys.* **1954**, *3*, 446–507.
33. V. Heine in *Solid State Physics* (Eds.: H. Ehrenreich, F. Seitz, D. Turnbull), Academic Press, New York, 1980, pp. 1–127, Vol. 35.
34. Y. Y. Tong, G. A. Martin, J. J. van der Klink, *J. Phys. Condens. Matter* **1994**, *6*, L533–L538.
35. G. Blyholder, *J. Phys. Chem.* **1964**, *68*, 2772–2778.
36. Y. Y. Tong, P. Mériaudeau, A. J. Renouprez et al., *J. Phys. Chem. B* **1997**, *101*, 10 155–10 158.
37. C. Rice, Y. Y. Tong, E. Oldfield et al., *J. Phys. Chem. B* **2000**, *104*, 5803–5807.
38. J. Wu, C. Coretsopoulos, A. Wieckowski in *Electrochemical Society Proceedings*, The Electrochemical Society, Pennington, NJ, 1997, pp. 426–442, Vol. 97-17.
39. D. K. Lambert, *Electrochim. Acta* **1996**, *41*, 623–630.
40. M. Weinert, A. J. Freeman, *Phys. Rev. B* **1983**, *28*, 6262–6269.